KAMBE, K. (1957). *J. Phys. Soc. Japan*, **12**, 13–31.
KOCH, F. & COHEN, J. B. (1969). *Acta Cryst* B**25**, 275–287.
LALLY, J. S., HUMPHREYS, C. J., METHERELL, A. J. F. & FISHER, R. M. (1972). *Phil. Mag.* **25**, 321–343.
MAGNÉLI, A., ANDERSSON, S., ÅSBRINK, S., WESTMAN, S. & HOLMBERG, B. (1958). Final Tech. Rept. No. 1, U. S. Dept. of Army, DA091-508-EUC-245 (September).
NORWOOD, T. F. & FRY, J. L. (1970). *Phys. Rev.* **B2**, 472–481.
REED, T. B. (1967). *Mater. Res. Bull.* **2**, 349–367.
REED, T. B. (1969). *Proc. Third Int. Symposium of High Temperature Technology*, Asilomar, California, pp. 655–664.
REED, T. B. & POLLARD, E. R. (1968). *J. Cryst. Growth*, **2**, 243–247.
REUTHER, V. H. & BRAUER, G. (1971). *Z. anorg. allgem. Chem.* **384**, 155–159.
RICHESSON, M., MORRISON, L., COHEN, J. B. & PAAVOLA, K. (1971). *J. Appl. Cryst.* **4**, 524–527.
SCHÖNBERG, N. (1954). *Acta Chem. Scand.* **8**, 221–225.
STENSTRÖM, G. & WESTMAN, S. (1968). *Acta Chem. Scand.* **22**, 1712–1714.
STIGLICH, J. J. JR, WHITMORE, D. H. & COHEN, J. B. (1973). *J. Amer. Ceram. Soc.* **56**, 211–213.
TAKEUCHI, Y. & SUZUKI, T. (1967). *J. Japan Inst. Metals*, **31**, 611–617.
TERASAKI, O., WATANABE, D., FUKAMACHI, T., HOSOYA, S. & SHIMIZU, M. (1972). *Phys. Lett.* **40A**, 357–358.
TEWARI, S. (1972). *Solid State Commun.* **11**, 1139–1142.
TOKONAMI, M. (1965). *Acta Cryst.* **19**, 486.
UYEDA, R. (1968). *Acta Cryst.* A**24**, 175–181.
UYEDA, R. (1974). *J. Appl. Cryst.* **7**, 1–18.
WATANABE, D., ANDERSSON, B., GJØNNES, J. & TERASAKI, O. (1974). *Acta Cryst.* A**30**, 772–776.
WATANABE, D. & TERASAKI, O. (1972). *Solid State Chemistry*, NBS Special Publication 364, Proceedings of 5th Materials Research Symposium, Edited by R. S. ROTH & S. J. SCHNEIDER, pp. 155–164.
WATANABE, D., UYEDA, R. & FUKUHARA, A. (1969). *Acta Cryst.* A**25**, 138–140.
WATANABE, D., UYEDA, R. & KOGISO, M. (1968). *Acta Cryst.* A**24**, 249–250.
WATSON, R. E. & FREEMAN, A. J. (1961). *Acta Cryst.* **14**, 27–37.
WESTMAN, S. (1960). Final Tech. Rept. No. 1, U. S. Dept. of Army, DA-91-591-EUC-1319.
WESTMAN, S. & NORDMARK, C. (1960). *Acta Chem. Scand.* 14, 465–470.

Acta Cryst. (1976). A**32**, 395

The Debye–Waller Factor of Nickel Measured at High Scattering Vectors by Pulsed Neutron Powder Diffraction

BY C. G. WINDSOR AND R. N. SINCLAIR

*Materials Physics Division, AERE, Harwell, Oxon OX*11 0*RA, England*

(*Received* 12 *September* 1975; *accepted* 16 *December* 1975)

The Debye–Waller factor of nickel has been measured by powder neutron diffraction over the range of scattering vectors Q from 10 to 24 Å^{-1} ($\sin\theta/\lambda$ from 0·8 to 2·0 Å^{-1}). Pulses of epithermal neutrons produced by the Harwell LINAC were scattered from a flat sample at nearly back-scattering angles ($2\theta = 150°$), and observed as a function of their wavelength determined from their time of flight over a 4·6 m flight path. The resolution in d spacing was observed to be nearly constant at about $\Delta d/d = 1\%$ over the above Q range. After background subtraction, calibration using a standard vanadium scatterer, and corrections for absorption, the powder pattern was analysed using the techniques of profile analysis, in which a computed powder profile is least-squares fitted directly to the observed profile. The profile refined to an χ^2 factor of 17%, giving a simple Debye–Waller factor $\exp(-2B\sin^2\theta/\lambda^2)$ with $B = 0{\cdot}34 \pm 0{\cdot}04$ Å^2. This value is appreciably less than the values of order 0·42 Å^2 obtained by neutron measurements at low Q. The inclusion of the fourth-order term $\exp(-2C\sin^4\theta/\lambda^4)$ predicted by anharmonic theory raised the fitted harmonic coefficient to $B = 0{\cdot}37 \pm 0{\cdot}04$ Å^2 in good agreement with X-ray and theoretical values, with $C = -0{\cdot}012 \pm 0{\cdot}006$ Å^4.

Introduction

The accurate determination of thermal and other parameters in crystallography depends to a considerable extent on the extension of Bragg intensity measurements to high values of the scattering vector $Q = 4\pi \sin\theta/\lambda$. This arises because the spatial resolution obtained from a structure refinement is directly related to the minimum value of the d spacings included. However data at high scattering vectors are not easy to obtain either with X-rays or with neutrons. With X-rays the problem is the fall off in the atomic structure factor with Q. For example in nickel, this is only around $\frac{1}{10}$ of its forward direction value at a Q of 10 Å^{-1} and this residual value is not known with great accuracy. With thermal neutrons of wavelengths close to 1 Å the maximum possible value of Q is limited to the value of about 12 Å^{-1} obtained in the back-scattering position. It follows that for higher values of Q shorter-wavelength or epithermal neutrons must be used. If these are produced conventionally by Bragg reflexion from a monochromating crystal, there are serious problems

from the loss of monochromator reflectivity with decreasing wavelength. In the case of powder spectroscopy the requirements of resolution dictate that the short-wavelength neutrons be delivered at a large take-off angle so that focusing techniques may be employed. This necessitates using a high-order monochromator reflexion with inevitably low reflectivity.

The advantages of a pulsed neutron source for Bragg intensity measurements were pointed out by Egelstaff & Squires (1954; Egelstaff, 1961) and Lowde (1956). The time-of-flight spectrum recorded by a counter at a fixed scattering angle gives the powder pattern as a function of increasing d spacing (Fig. 1). The method has been used for thermal-energy measurements by many authors both using reactor sources (Buras *et al.*, 1964; Brugger, Bennion & Worlton, 1967; Reichelt & Rodgers, 1966; Schwartz, 1966; Lebech & Mikke, 1972) and using LINAC sources (Moore, Kasper & Menzel, 1968, Kimura *et al.*, 1968). The use of a LINAC as the pulsed neutron source gives the advantage of a relatively large epithermal neutron flux compared to that from a reactor source. Also if suitably thin or poisoned moderators are used, the neutron pulse time can be made proportional to the wavelength giving a d-spacing resolution $\Delta d/d$ independent of Q, as we shall demonstrate theoretically and experimentally in the next section.

As was emphasized by Maier-Leibnitz & Springer (1966), the use of a nearly back-scattering configuration enables the contribution to the resolution from the counter aperture to be made very small and recent measurements by Steichele & Arnold (1973) using a pulsed reactor beam have confirmed the very high resolutions obtainable in this configuration. A LINAC pulsed source offers the further advantage that it becomes possible to match the large counter aperture with a large source aperture. In practice beam-chopping rotors giving pulse times comparable to those from a LINAC source have limited aperture and transmitted solid angle.

The prime disadvantages of the time-of-flight method are that the incident wavelength distribution must be independently determined and that the absorption and other corrections must be made at varying wavelengths. It was a primary objective of the present study to show that these factors could be adequately allowed for. When discussing the thermal parameters we shall use the term Debye–Waller factor to denote the function $\exp(-2W)$. The Debye–Waller parameter W will be divided into a harmonic contribution $B\sin^2\theta/\lambda^2$, where B is the harmonic coefficient, and an anharmonic series of terms with higher even powers of $\sin\theta/\lambda$. However we shall only consider the quartic term $C\sin^4\theta/\lambda^4$ and C will be termed the anharmonic coefficient.

Resolution considerations

We shall show that spectrometers whose overall pulse time is dominated by the epithermal neutron moderation time give a resolution $\Delta d/d$ independent of wavelength.

In the time-of-flight method d spacings are deduced by measuring the time of flight T of neutrons traversing a total flight path $L=L_0+L_1$ (see Fig. 1) using a counter at a fixed scattering angle 2θ. From Bragg's law we obtain for the d spacing in terms of Planck's constant h and the neutron mass m

$$d=\frac{\lambda}{2\sin\theta}=\frac{hT}{2mL\sin\theta}. \tag{1}$$

Differentiation of this equation to find the fractional error in the d spacing gives

$$\frac{\Delta d}{d}=\frac{\Delta T}{T}+\cot\theta\Delta\theta+\frac{\Delta L}{L}. \tag{2}$$

Considering the first term, the time spread ΔT is strictly a convolution of the neutron thermalization time and the electron pulse time. On our optimized system the electron pulse time is only 1·7 μs so that in the wavelength range of the present experiment (above 0·5 Å) ΔT approximates closely to the neutron thermalization time. It has now been demonstrated that in suitably thin, poisoned or cooled moderators the build up of a Maxwellian neutron distribution is prevented or shifted to cold-neutron energies. The neutron-thermalization pulse times within this extended epithermal region can then be made for neutrons of wavelength λÅ or energy E eV (Day & Sinclair, 1969; Fluharty, Simpson, Russell & Menzel, 1969) of order

$$\Delta T\simeq 7\lambda\,\mu\text{s}\simeq\frac{2}{\sqrt{E}}\,\mu\text{s}. \tag{3}$$

The total flight time of the neutrons is also proportional to wavelength

$$T=\frac{h}{m}L\lambda=\frac{L\lambda}{3{\cdot}95603}\,\mu\text{s} \tag{4}$$

if L is expressed in mm. The fractional error in the time is therefore independent of wavelength

$$\frac{\Delta T}{T}=\frac{7h}{mL}=\frac{28}{L}. \tag{5}$$

Since the other two terms $\cot\theta\Delta\theta$ and $\Delta L/L$ are also independent of wavelength, the d-spacing resolution $\Delta d/d$ for the whole spectrometer is independent of wavelength throughout the epithermal region. This is

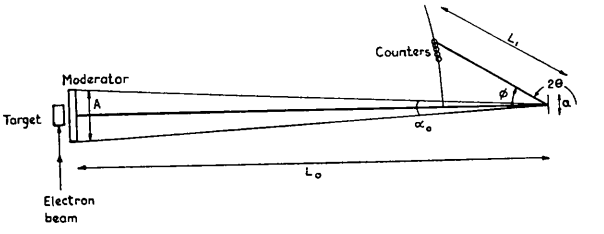

Fig. 1. Schematic layout of a time-of-flight powder spectrometer.

in contrast to a conventional two-axis spectrometer operating on a reactor where the resolution improves rapidly with increasing Q up to a focusing angle where the monochromator and sample scattering angles are approximately equal, but then deteriorates with further increase in Q. It also contrasts with a rotor time-of-flight spectrometer having a rotor pulse time ΔT independent of wavelength so that the resolution at small d spacings becomes dominated by the pulse-time uncertainty and eventually deteriorates linearly with increasing Q. These differences are illustrated in Fig. 2, where we compare the resolution $\Delta d/d$ observed in the present LINAC experiment with unpublished information of the resolutions from the PANDA spectrometer at Harwell and the time-of-flight spectrometer at Garching. The points represent data deduced from the widths of individual peaks in the nickel spectrum shown later in Fig. 4, and the solid line is deduced from the widths assumed in the profile-analysis fit. The LINAC resolution is shown to remain broadly constant even up to scattering vectors near 20 Å^{-1}, which is nearly double the maximum given by PANDA with a 90° take-off angle and a germanium 333 monochromator.

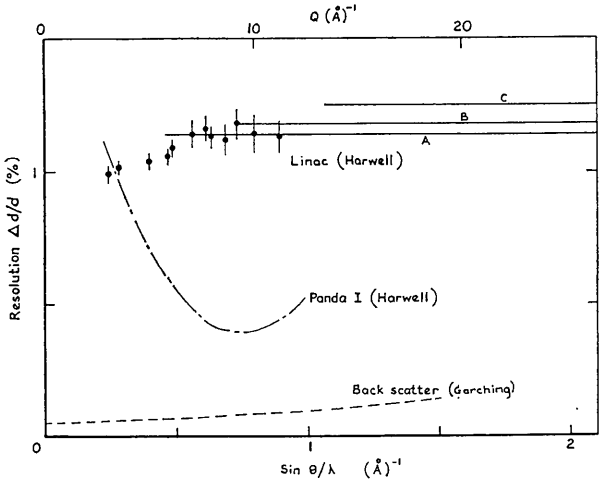

Fig. 2. The observed resolution $\Delta d/d$ as a function of scattering vector.

Spectrometer design considerations

The spectrometer and sample geometry were chosen for this experiment to optimize the count rate at given resolution using the back-scattering geometry. We now give the design criteria used and show in Table 1 the relevant dimensions which can be derived from the requirement of a given d-spacing resolution $R=\Delta d/d$. We assume a pulsed neutron source giving pulses of length ΔT over an area A^2, with a sample area a^2. The criterion chosen was to match the three contributions to the resolution given in equation (2) so that in terms of root-mean-square values

$$\frac{\Delta T}{T}=\cot\theta\Delta\theta=\frac{\Delta L}{L}=\frac{R}{\sqrt{3}}. \tag{6}$$

This approach is much less general than that given by Buras & Holas (1966) where all parameters were adjusted simultaneously to optimize the intensity. However it does enable expressions for several instrumental parameters to be derived analytically and discussed as a function of the specified wavelength and resolution. The total flight path is then given by

$$L=\frac{hT}{m\lambda}=\frac{\sqrt{3}h\Delta T}{m\lambda R}. \tag{7}$$

It is seen from Table 1 that for epithermal-moderation pulse times the total flight-path length L for a 1% resolution spectrometer is 4·8 m independent of wavelength. The allowable error in the neutron flight path ΔL is similarly given by

$$\Delta L=\frac{h\Delta T}{m\lambda}. \tag{8}$$

It is thus independent of resolution and for epithermal-moderation pulse times is also independent of wavelength, having a value of 28 mm. This of course matches the distance covered by a neutron in its moderation time. For our present case of a plate sample the distance error arising from sample size is negligible so that ΔL should be matched to the counter size. One-inch diameter cylindrical counters are therefore suitable. The horizontal angular divergence (α_0) which is

Table 1. *Parameters of matched time-of-flight spectrometers*

Parameter	Resolution R	Wavelength λ (Å)	Pulse time ΔT (μs)	Flight path L (m)	Distance error ΔL (mm)	Incident collimation α_0 (°)	Maximum back-scatter ϕ_{max} (°)	Scattered flight path L_1 (m)
Equation				(7)	(8)	(9)	(11)	(14)
LINACS	1%	½	3·5					
		1	7	4·80	28	1·2	31·7	0·44
		2	14					
	0·3%	1	7	14·4	28	0·36	31·7	1·31
	0·1%	1	7	48·0	28	0·12	31·7	4·36
This experiment				4·566	25	1	35	0·4
Reactor	1%	0·5	20	27·4	79	0·21°	104	2·5
		1	20	13·7	79	0·42°	104	1·25

Assumptions: Source area 100 × 100 mm; sample area 25 × 25 mm.
LINAC pulse time 7λ Å^{-1}; reactor pulse time 20 μs.

frequently the determining factor in the incident-beam intensity is given generally from the flight path. Providing we make the commonly satisfied conditions of small sample to moderator dimensions ($a \ll A$) and a short scattered flight path ($L_1 \ll L_0$) then

$$\alpha_0 \simeq \frac{A}{L} = \frac{Am\lambda R}{\sqrt{3}h\Delta T}. \tag{9}$$

This gives a 1° angular aperture for the 1 % resolution case. The incident angular collimation α_0 determines completely the angular deviation in the scattering angle $\Delta\theta$, since the time-focusing technique of Graham & Carpenter (1970) may be used to adjust the scattered-beam path length to compensate for changes in scattering angle. The minimum allowed value for the scattering angle is therefore given by

$$\cot\theta_{\min} = \frac{R}{\sqrt{3}\alpha_0} = \frac{h\Delta T}{Am\lambda}. \tag{10}$$

Expanding $\cot\theta$ in terms of the angle away from back scattering (ϕ) gives

$$\phi_{\max} \simeq 2\cot\theta_{\min} = \frac{2h\Delta T}{Am\lambda} = \frac{2\Delta L}{A}. \tag{11}$$

This is again independent of resolution and wavelength in the LINAC case and works out at around 32°. In terms of an expansion in ϕ, the time-focused scattered neutron flight path at an angle ϕ may be written as

$$L_1(\phi) = L_1(0)\sec\phi + \frac{\phi^2}{8}(L_0 - 3L_1) - \frac{\phi^4}{384}(75L_1 - 5L_0). \tag{12}$$

Thus in the case of $L_1 = \frac{1}{3}L_0$ the counter array may be essentially planar. This is often inconveniently large however, and in general the minimum scattered-flight path length which can be permitted depends on the change in scattered-neutron flight path between neutrons scattered from either side of the sample of width a to counters at the maximum angle $\phi_{\max}$,

$$\Delta L_1 = \frac{a}{L_1}\frac{dL_1}{d\phi} \simeq \frac{a\phi_{\max}}{4}\left(\frac{L_0 - 3L_1}{L_1}\right). \tag{13}$$

Matching this error to the allowed ΔL of equation (9) leads to a minimum scattered flight path

$$L_1 = \frac{L_0}{3 + 2A/a} \tag{14}$$

which works out at 0·44 m for the LINAC with 1 % resolution. Table 1 shows how well the basic parameters of the spectrometer used for this experiment correspond with those predicted from our criterion with a specified 1 % resolution. The table shows how readily the LINAC method can be extended to higher resolutions. It also shows that the method is difficult to extend to short wavelengths using a reactor and rotor to give the pulsed neutrons. With a 20 μs burst time, flight paths of 27 m are needed with 0·5 Å neutrons. The use of guide tubes is not suitable since at these wavelengths a nickel guide has an appreciably smaller acceptance angle than that given by the incident solid angle.

Experimental

The experiment was performed on an adapted version of the Harwell LINAC Total Scattering Spectrometer (Sinclair *et al.*, 1974) (see Fig. 3). The electron target produces around 2×10^{13} fast neutrons per second in 1·7 μs pulses at 192 pulses per second. The fast neutrons were then moderated in a 'cadmium sandwich' heterogeneously poisoned moderator composed of a 20 mm polyethylene slab separated by a 1 mm cadmium sheet from a 6 mm polyethylene slab. Such a moderator allows the full 26 mm thickness of polyethylene to be effective in slowing down the fast neutrons of energy greater than the cadmium transmission cut-off of about 0·5 eV, but allows only the 6 mm thickness to be effective in slowing down neutrons of lower energy. This effectively prevents the build up of any appreciable Maxwellian distribution in the moderator, as is shown in Fig. 4(*a*) by the absence of any thermal peak in the incident spectrum as measured by a standard vanadium incoherent scatterer. The absence of a Maxwellian distribution also prevents the occurrence of any significant pulse broadening beyond the thermalization time broadening of equation (3). This was illustrated by the wavelength-independent resolution

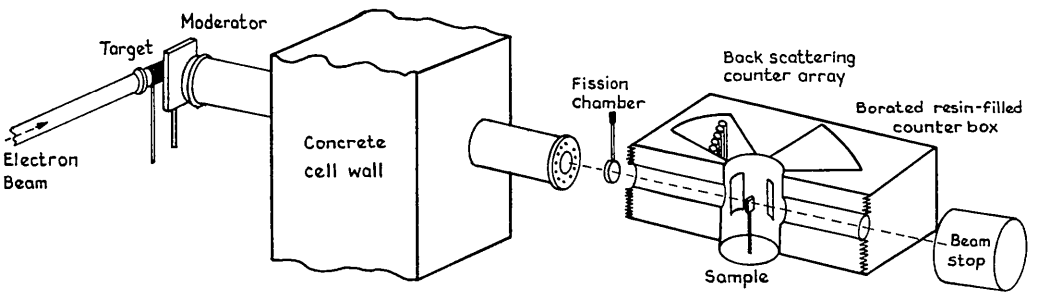

Fig. 3. The general arrangement of the Harwell Total Scattering Spectrometer.

shown in Fig. 2 which implies a pulse broadening proportional to wavelength. For 1 Å neutrons the measured pulse-time broadening, which includes contributions from the finite angular and distance resolution, was 10 μs compared with 15 μs obtained from a conventional 25 mm polythene slab moderator, and the exponential tail on the long-wavelength side of the pulse was largely removed. These advantages were obtained at the cost of an order of magnitude intensity reduction over the conventional moderator to give a 1 Å flux at the moderator surface of around $4 \cdot 10^9$ n $cm^{-2}\ s^{-1}\ eV^{-1}$.

The nickel powder sample was encased in a container of flat-plate geometry and size $31 \times 43 \times 2$ mm. It had a front window of vanadium foil weighing 0·029 g cm^{-2} and scattering only 1·8% of the beam. Its sides and rear face were of cadmium. It contained 1·02 g cm^{-2} of powder and scattered 16% of the beam.

The counter bank was centred at 150° scattering angle but extended from 143° to 158°. It consisted of six 25 mm diameter ^{3}He counters stopped down to an active length of 150 mm and inclined at an angle of 39° to the scattered beam direction to give time focusing. The effective counter-bank area was therefore 96×150 mm at a distance of 400 mm giving an effective solid angle of 0·09 rad^2.

Fig. 4(*a*) shows an example of the observed spectrum from the nickel powder points together with the spectrum from a standard vanadium plate sample of thickness 2 mm giving 6·6% scattering (full line) and the background spectrum with no sample or can present (dashed line). It is seen that the instrumental background is small compared to the incoherent-scattering contribution from the nickel powder. At $\sin\theta/\lambda$ of 1 Å^{-1} the instrumental background is around one quarter of the incoherent signal but this fraction rises to around a half at $\sin\theta/\lambda$ of 0·25 Å^{-1}. The 'booster peak' in the centre of the spectrum is a background from the adjacent neutron booster which is multiplexed with our target.

Presentation of the powder profile as a differential cross section

A conventional fixed-wavelength powder profile has the desirable property that it is proportional to the differential cross section ($d\sigma/d\Omega$). Thus any incoherent-scattering cross section gives simply a flat contribution to the background. We have processed the time-of-flight profile to give it in a similar form using the program *LINDA* (Clarke, 1975) originally written for the analysis of spectra from liquids. This program normalizes the various spectra according to a count rate recorded by a fission chamber monitoring the incident beam, subtracts the appropriate background spectra after performing absorption corrections, and finally calibrates the spectrum with respect to that from a standard vanadium sample assumed to have a constant cross section $\sigma = 5 \cdot 13$ barn. Using the suffixes *S*, *V*, *C* and *B* to denote the sample, vanadium, can and background contributions, the programme evaluates

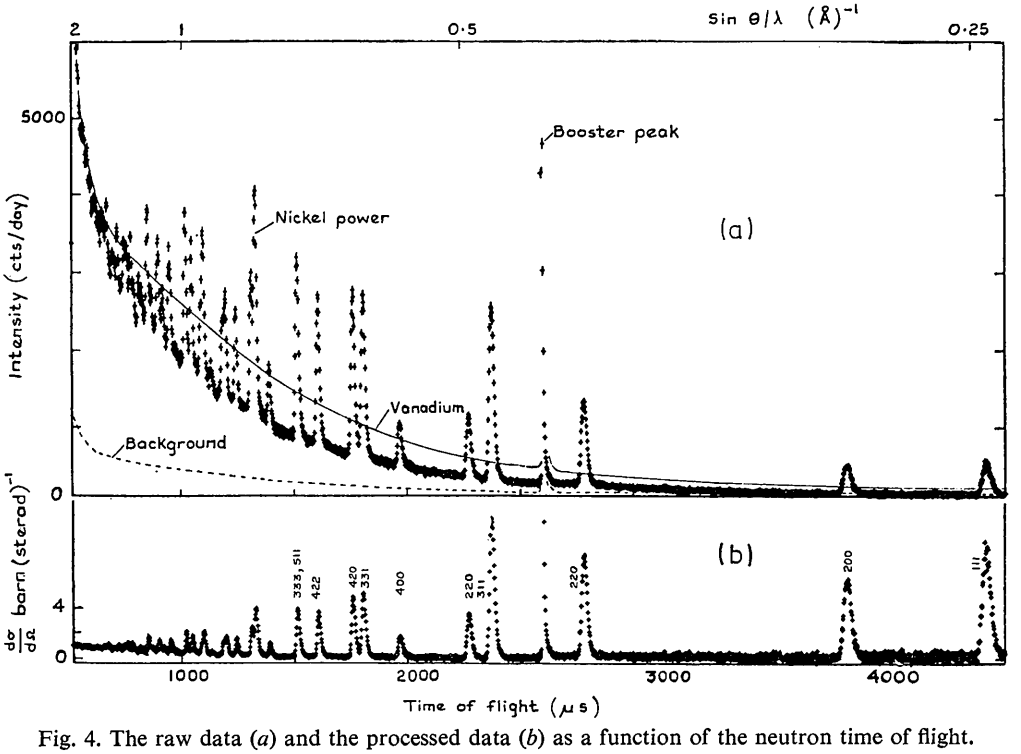

Fig. 4. The raw data (*a*) and the processed data (*b*) as a function of the neutron time of flight.

$$\frac{d\sigma}{d\Omega}=\frac{N_V}{N_S}\frac{\sigma_V}{4\pi}\left[\left(\frac{I_{S+C}}{m_{S+C}}-\frac{I_B}{m_B}\right)\frac{1}{A_{SS}}-\left(\frac{I_C}{m_C}-\frac{I_B}{m_B}\right)\frac{A_{CS}}{A_{SS}A_{CC}}\right]\Big/\left(\frac{I_{V+B}}{m_{V+B}}-\frac{I_B}{m_B}\right)\frac{1}{A_{VV}}, \quad (15)$$

where I represents the recorded spectra, m the monitor counts, N the number of atoms, and the A terms are absorption corrections evaluated using the method of Paalman & Pings (1962). This absolute cross section is shown in full in Fig. 4(*b*) and used in all the profile-fitting procedures described and presented in the rest of the paper.

We now consider the integrated intensities of all powder reflexions measured on a time-of-flight spectrometer and presented in the form of a differential cross section. Following Marshall & Lovesey (1971), equation (2.41), the cross section per unit cell may be written

$$\sigma_l=\frac{4\pi^3 z_1}{k^2 v_0 Q}|F_1|^2 \quad (16)$$

where z_1 is the multiplicity of the lth-order peak, F_1 the unit-cell structure factor and v_0 the unit-cell volume. This equation may be written

$$\sigma_l=\frac{\lambda^3 z_l}{4v_0\sin\theta}|F_1|^2, \quad (17)$$

showing the familiar λ^3 variation of the integrated cross section as a function of wavelength responsible for the general form of time-of-flight profiles (Buras, 1963). The observed integrated neutron intensity of the lth reflexion I_l, will depend on the incident flux per unit wavelength $i(\lambda)$, the wavelength spread accepted by the counter $\Delta\lambda$, and the fraction of the Debye–Scherrer ring intercepted by the counter f, according to

$$I_l=N_S\sigma_l i(\lambda)\Delta\lambda f, \quad (18)$$

where N_S is the number of unit cells in the sample lying within the beam and where the accepted wavelength spread $\Delta\lambda$ is related to the angular acceptance of the counter bank $\Delta\theta$ according to

$$\Delta\lambda=\lambda\cot\theta\Delta\theta. \quad (19)$$

Similarly with the vanadium specimen we may write for the intensity observed in a particular time channel whose width δT corresponds to another wavelength interval $\delta\lambda$

$$I_V=N_V\sigma_V i(\lambda)\delta\lambda\Delta\Omega/4\pi, \quad (20)$$

where from equation (4)

$$\delta\lambda=\frac{h}{mL}\delta T \quad (21)$$

and where the solid angle subtended by the counter $\Delta\Omega$ is given by

$$\Delta\Omega=f2\pi\sin(2\theta)\Delta(2\theta). \quad (22)$$

Thus the integrated reflexion intensity observed in a time-of-flight spectrum with channel width δT and processed using equation (15) to give unit differential cross section is given by

$$\frac{d\sigma}{d\Omega}=\frac{1}{4\pi}\cdot\frac{N_V\sigma_V}{N_S}\cdot\frac{I_l}{I_V}=\frac{1}{8\pi}\frac{\lambda\sigma_l}{\sin^2\theta}\cdot\frac{mL}{h\delta T}. \quad (23)$$

Substituting equation (16) for σ_l we obtain finally

$$\frac{d\sigma}{d\Omega}=\frac{1}{32\pi^2}\frac{\lambda^4 z_l}{v_0\sin^3\theta}\frac{mL}{h\Delta T}|F_1|^2. \quad (24)$$

This equation may also be written in terms of d spacings as

$$\left(\frac{d\sigma}{d\Omega}\right)_l=\frac{1}{2\pi}\frac{d_1^4 z_l\sin\theta}{v_0}\frac{mL}{h\Delta T}|F_1|^2. \quad (25)$$

In our special case of nickel having a face-centred cubic structure with one atom in the primitive unit cell the structure factor depends only on the coherent cross section $\sigma^{\rm coh}$, and the Debye–Waller factor $\exp(-2W)$ and the integrated intensity for the hklth reflexion reduces to

$$\left(\frac{d\sigma}{d\Omega}\right)_{hkl}=\frac{2}{\pi}\frac{\sigma^{\rm coh}}{4\pi}a_0\sin\theta\frac{mL}{h\Delta T}\times\left[\frac{z_l}{(h^2+k^2+l^2)^2}\exp(-2W)\right]. \quad (26)$$

For spectra observed at a given angle, only the terms in the bracket vary with order, and apart from the Debye–Waller factor, these take the form of a rational fraction which can be calculated exactly.

The profile-analysis procedure

In structural refinement studies with powders the object is to find the integrated intensities of the various order reflexions. When these are separated by at least some distance of uniform background, their intensities may be reliably evaluated by summation over the region of the peak followed by subtraction of a background contribution. This is generally possible only for the lower orders since, as shown for example in Fig. 4(*b*), the higher orders overlap to give a continuous spectrum. It is in this region that the technique of profile analysis has been shown to be of great value in conventional fixed-wavelength powder spectroscopy (Rietveld, 1969; Hewat, 1973). We now consider the adaptation of their techniques to the case of time-of-flight powder measurements using a LINAC.

A simplified flow diagram of the profile-fitting procedure used is shown in Fig. 5. First the d spacings d_l and multiplicities z_l for each order l are calculated and arranged in descending order of d spacing down to some specified minimum value $d_{\rm min}$. Secondly the observed profile y_i(obs) and its error Δy_i(obs) are read

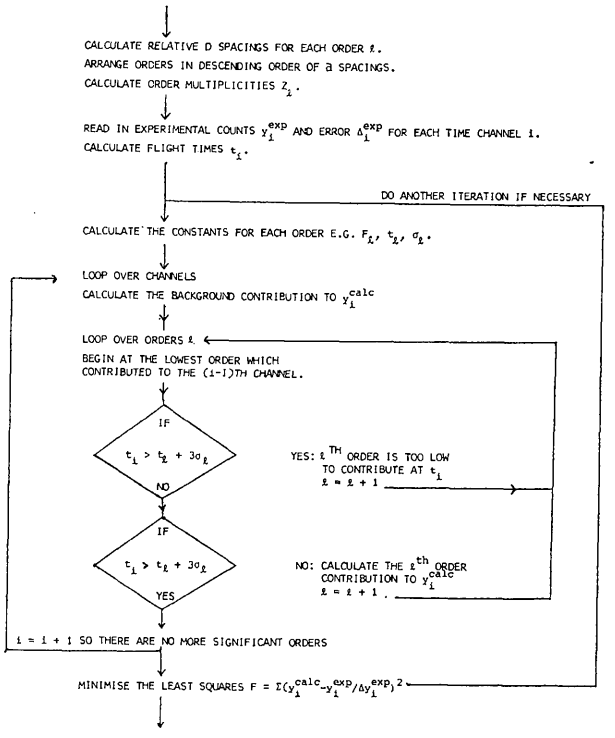

Fig. 5. A simplified flow diagram of the profile-fitting program.

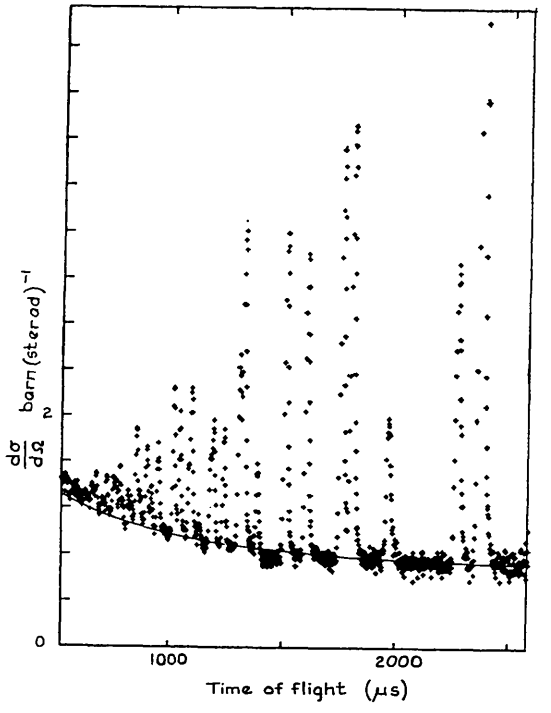

Fig. 6. The time-of-flight cross section shown on an expanded scale to illustrate the variation in the background. The solid line shows the background generated by fit *A* (see Table 5).

in for each time channel i, and the corresponding flight times t_i calculated. The program then enters the least-squares fitting procedure in which the experimental profile is fitted to a calculated profile y_i(calc) by minimizing the sum of deviations

$$\chi^2 = \frac{1}{M-N}\sum_{i=1}^{M}\left[\frac{y(\text{obs})-y(\text{calc})}{\Delta y_i(\text{obs})}\right]^2 \qquad (27)$$

with respect to the N parameters X_j of the calculated profile which we wish to determine. In practice, we have performed this minimization using the Harwell subroutine *VAO2A* by Powell (1965). The calculated profile at the ith time channel is in general composed of a background contribution y_i(bg) and a sum of contributions $f_l y_i(l)$ from orders l sufficiently close to give a significant contribution to the ith channel:

$$y_i(\text{calc}) = y_i(\text{bg}) + \sum_l f_l y_i(l)\,. \qquad (28)$$

As in Reitveld's programme, the test of significance is taken that the flight time corresponding to the lth order t_l differ from the flight time of the ith channel t_i by some specified amount, here taken as $3\sigma_l$ where σ_l is the standard deviation of the lth order:

$$|t_l - t_i| \le 3\sigma_l\,. \qquad (29)$$

Our programme differs from Reitveld's in not requiring a separate profile-preparation programme to be run giving this significant reflexion list for each channel. This list is generated by beginning the profile calculation with the longest time channel where the summation over l in equation (28) must begin with the lowest order. However for each subsequent channel the summation begins with the lowest order which gave a significant contribution to the previous time channel. Since the reflexions have been ordered with descending d spacings, the summation may be concluded when an order more than $3\sigma_l$ above t_i is found. The parameters necessary for the description of the calculated profile will now be described in more detail.

(1) *The background description*

In Fig. 6 the differential cross section from the first half of Fig. 4(*b*) is shown on an enlarged scale to emphasize the background profile. At large times the profile is seen to approach a constant background level presumably reflecting incoherent scattering from the sample. However at smaller times the background rises considerably. We assume that this effect is caused by inelastic scattering which may, to a first approximation, be treated within an incoherent approximation and assumed to increase the background. The conventional Debye–Waller factor represents the loss of Bragg reflexion intensity to processes of this kind so that we might expect a background contribution of the form

$$y_i(\text{bg}) = \left(\frac{d\sigma}{d\Omega}\right)_{\text{inc}} + \left(\frac{d\sigma}{d\Omega}\right)_{\text{coh}}[1-\exp(-2W)]\,. \qquad (30)$$

In practice we introduce adjustable parameters for each term in this equation, and have fitted the background contribution to

$$y_i(\text{bg}) = X_1 + X_2[1 - \exp(-2X_3 \sin^2\theta/\lambda^2)] . \quad (31)$$

The solid line in Fig. 6 shows a background contribution of this type given by one of the full profile fits.

(2) *The line-shape description*

The line shapes observed throughout the spectrum have two outstanding features: their general width increases roughly linearly with time as implied by equation (3), and they are asymmetric, having a more gradual trailing time than their rise time, as illustrated clearly in Fig. 7. A full analysis of this line shape might be possible by reproducing the full equations for neutron moderation. However, we have chosen the simple asymmetric Gaussian

$$y = \frac{1}{2\pi\sigma_t}\left(\frac{2X_4}{1+X_4}\right) \exp\left[-\frac{G}{2\sigma_t^2}(t_i - t_l)^2\right], \quad (32)$$

where G equals the asymmetry parameter X_4 for the leading edge $t_i < t_l$ and is put equal to unity for the trailing edge $t_i > t_l$. As can be seen from the solid line in Fig. 7, such a curve fits the experimental profile reasonably well. The curve has unit integrated area, and a full width at half height

$$w = 2{\cdot}354\sigma(1+X_4)/2X_4 . \quad (33)$$

This width w is further assumed to be proportional to the wavelength as in equation (3) but with another parameter X_5 as proportionality constant:

$$w = X_5\lambda . \quad (34)$$

(3) *Peak-position determination*

The flight times t_l at which the peaks are observed are generally determined by the total flight path L and the unit-cell lattice constants and angles which define the d spacing d_l for each order. Although the zero of the time scale is given in principle by the firing time of the LINAC, there is in practice a small delay between this time and the peak time of the moderated neutron pulse. A wavelength-independent delay of this sort, which may also arise from delay in the neutron counter, may readily be deduced from the form of the spectrum alone. A parameter X_7 has therefore been introduced describing the apparent delay, of about 6 μs only, between the LINAC pulse and the zero of the spectrum. Any delay caused by neutron thermalization is likely to be proportional to the wavelength. This cannot be fitted as a parameter since the neutron flight time is itself proportional to wavelength and so the correction implies simply a scaling of the lattice parameters. However the full width at half height of the neutron thermalization time is well established to have the form given by equation (3). We suppose the delay to be given by this full width divided by the asymmetry factor as sketched in Fig. 7. The expression for the observed flight time in μs with respect to the LINAC start pulse is therefore

$$t_l = d_l \frac{2\sin\theta \,.\, mL}{h} + X_7 + \frac{7\lambda}{X_4}$$
$$= d_l\, 2\sin\theta\left(\frac{mL}{h} + \frac{7}{X_4}\right) + X_7 . \quad (35)$$

In our case with a flight path of 4·6 m and an asymmetry factor of about 1·6, the wavelength-dependent delay decreased the lattice parameter by a factor 0·99615. In our case of nickel with a cubic structure the d spacings are determined by only one parameter $X_6 = a_0$, and the flight times become

$$t_l = \frac{X_6}{(h^2+k^2+l^2)^{1/2}} 2\sin\theta\left(\frac{mL}{h} + \frac{7}{X_4}\right) . \quad (36)$$

(4) *Peak-intensity description*

The form of the integrated intensity of the various orders has been given in equation (25) and will in general involve many structural and thermal parameters. However in the present case of a cubic material with one atom per unit cell equation (26) is valid and we may describe the peak intensities by a overall scaling factor relating to the coherent-scattering cross section $X_8 = \sigma^{\text{coh}}/4\pi$ per steradian, and a harmonic coefficient $B = X_9$:

$$f_1 = \frac{2}{\pi} a_0 \sin\theta \frac{mL}{h\delta T} \frac{z_1}{(h^2+k^2+l^2)^2}$$
$$\times X_8 \exp(-2X_9 \sin^2\theta/\lambda^2) . \quad (37)$$

For some fits it was found necessary to add a further term to the Debye–Waller factor involving the fourth

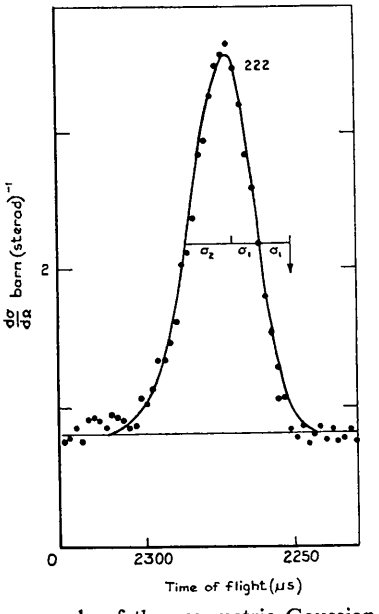

Fig. 7. An example of the assymetric Gaussian peak profile. The arrow shows the assumed initial time of the pulse.

power of $\sin\theta/\lambda$ and introducing a new parameter X_{10} so that the Debye–Waller factor in (37) becomes

$$\exp(-2X_9\sin^2\theta/\lambda^2-2X_{10}\sin^4\theta/\lambda^4). \quad (38)$$

(5) *Extinction*

It is not usually necessary to consider extinction in conventional fixed-wavelength powder spectra, but the λ^4 dependence of the time-of-flight powder-pattern intensities means that the correction is almost bound to become important in the very long wavelength end of a back-scattering powder spectrum. This is no real problem since these low-order peaks are easily measured at ordinary wavelengths by using lower-angle counters, or by using a conventional spectrometer. If these low-order peak intensities are known then an extinction correction can be readily estimated and applied to the more important high-order peak intensities. Of course, the λ^4 intensity dependence of the time-of-flight intensities means that the extinction effects are equally bound to become negligible in the important region of high $\sin\theta/\lambda$.

Extinction has been discussed generally by Zachariasen (1967) and more recently by Becker & Coppens (1974). It may be divided into primary extinction, the attenuation of the beam within a mosaic block of a crystallite; secondary extinction, the attenuation of the beam within a crystallite, and self-shielding, the attenuation of the beam through the powder.

This last effect is not difficult to calculate for our simple geometry if the powder cross section (σ_l) of equation (17) is known. If there are N atoms per unit volume, the incident beam is attenuated by a factor $\exp(-N\sigma x)$ at distance x within the crystal. The scattered beam at angle 2θ is further attenuated by exp $[N\sigma x\sec(\pi-2\theta)]$ on leaving the crystal so that the measured intensities for a flat plate of thickness t are reduced by

$$y_{ss}=\frac{1-\exp\{-N\sigma t[1+\sec(\pi-2\theta)]\}}{[1+\sec(\pi-2\theta)]N\sigma t}. \quad (39)$$

An approximate expression for the scattering cross section is given in (17) on substituting for F^2 and v_0 by

$$\sigma_l=\frac{\lambda^3 z_l F^2}{4v_0\sin\theta}=8\sin^2\theta\frac{\sigma^{\rm coh}}{4\pi}\left[\frac{z_l\exp(-2W)}{(h^2+k^2+l^2)^{3/2}}\right]. \quad (40)$$

This correction thus varies as λ^3 rather than as the λ^4 variation of the peak intensities, the difference arising from the 'wavelength window' which is itself proportional to the wavelength. If a value for $\sigma_{\rm coh}$ is known, as in the case of nickel, this correction may be evaluated without introducing any adjustable parameters.

The primary and secondary extinction effects are often treated by the particularly simple approximation of assuming a diminution of intensities proportional to the intensities themselves. Thus the correction factors reducing the intensities f_l of equation (37) have the form

$$y_{\rm ext}=1-X_{11}\left[\frac{z_l\exp(-2W)}{(h^2+k^2+l^2)^2}\right], \quad (41)$$

where the parameter X_{11}, which is in reality determined by a mixture of mosaic block, crystallite and sample sizes, is treated as an adjustable parameter to be fitted by experiment. This equation is similar to equation (39) with the exponential expanded to second order. However it is not identical since the correction factor has the same λ^4 variation as the observed intensities. This sharp variation allows the parameter to be readily determined in practice from the first few orders.

(6) *Thermal diffuse scattering (TDS)*

This refers to the inelastic scattering processes of phonon annihilation and creation. Because single-phonon cross sections are larger close to Bragg reciprocal-lattice points, its effect can be to cause a wing beneath each powder pattern peak, which if included in the Bragg intensity would result in an incorrect structure factor. The effect is well known in fixed-wavelength single-crystal studies, but is generally small for powders, although it may become important in the present work because of the general increase in phonon cross sections with Q^2. In the case of powder patterns measured at constant wavelength a detailed discussion of the TDS correction has been given by Chipman & Paskin (1959). The case of time-of-flight fixed-angle powder patterns is quite different, both because the integration scan over reciprocal space is dif-

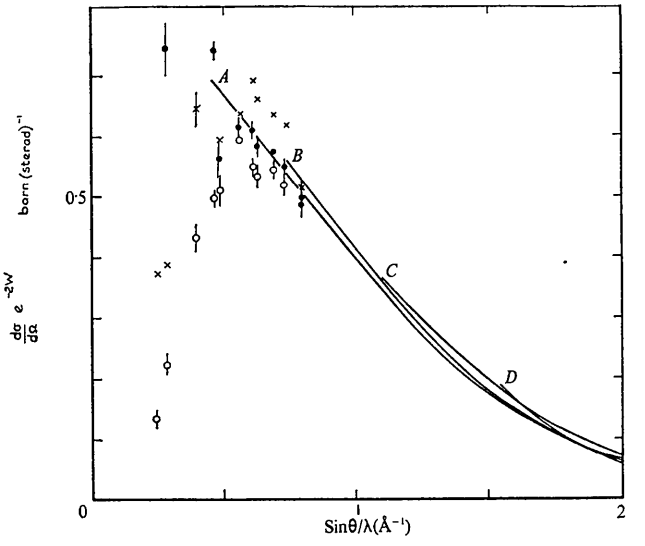

Fig. 8. The measured cross section $(d\sigma/d\Omega)_{\rm coh}\exp(-2W)$ plotted as a function of $\sin\theta/\lambda$. The points represent data from individual Bragg peaks: the closed circles representing data with an extinction parameter, the crosses data corrected only for self-shielding, and the open circles data without correction. The solid lines represent the profile analysis fits represented in Table 4.

ferent and because of the differing effects incident- and scattered-neutron energy changes have on the elapsed time of flight. A detailed discussion is beyond the scope of this paper and must be postponed till a later paper. However we give the following argument, not to show that TDS is small, but rather to show that its effects at high Q are broad on a time-of-flight scale and so are taken into account by the background contribution mentioned in the first section of this paragraph. As Chipman & Paskin point out, even the one-phonon TDS contributions, which peak at the Bragg positions, overlap appreciably so that their effect depends on the span of the spectrum used to determine the background. The two-phonon TDS contribution is almost flat and has only singularities of slope at the Bragg positions. Third- and higher-order phonon contributions will be even more featureless. The contribution of the two-phonon term compared with single-phonon terms rises as the Debye–Waller factor falls, so that, at the highest Q ranges of this experiment where the Debye–Waller factor has fallen to only one tenth, the contribution of the single-phonon TDS contribution with its undesirable peaks at the Bragg positions will have become negligible compared with the more featureless multiphonon TDS contributions.

The low-order results

We first consider the intensities of the lower-order peaks in the time-of-flight spectrum. The first 11 orders, up to 440, are nearly all separated by a well defined background region so that their intensities may be evaluated by a simple summation and background subtraction without resorting to a profile-analysis procedure. Even slightly overlapping peaks such as the 420,331 pair could be reliably estimated by applying a small correction for the overlapping intensity. The background level under each peak was estimated by averaging the backgrounds observed beyond its wings. In Table 2 we show the area of each order in the measured unit of barns per steradian microsecond which we then convert into $\sigma^{\text{coh}} \exp(-2W)/4\pi$ by multiplication by the known factors given in equation (26). The figures in brackets are the estimated errors which in fact arise mainly from the uncertainty in the background. These points are plotted in Fig. 8 as the open circles and show the essential need for some extinction or self-shielding correction in the orders measured at wavelengths greater than 1·5 Å. The curves in this figure correspond to the profile fits of Table 4. The longest curve (A) corresponds to a harmonic Debye–Waller factor with $B=0{\cdot}34$ Å^2. The crosses show the values obtained by applying the self-shielding correction term of equation (40). The low-order peaks are much closer to the expected intensity variation but the method appears to 'over-correct' the situation so that low-multiplicity orders like 400 and 440 lie below the trend, while high-multiplicity orders like 311 are above it. The closed circles in the figure show the much improved trend given by applying equation (41) with the parameter X_{11} adjusted to the value 2·0. This gave a 30% correction around 2·4 Å but essentially negligible corrections (mostly below 2%) below 1·2 Å.

It is seen that the results from the low-order peaks below about $\sin\theta/\lambda$ of 0·5 Å^{-1} are rather too heavily affected by extinction effects to be useful in themselves, but give excellent data for applying an increasing small correction factor to the data at higher values of $\sin\theta/\lambda$.

Profile fitting results

The fitting was performed on the Harwell IBM 370/75 computer. A 1000-point spectrum with nine parameters achieved convergence after around 13 iterations and some 14 s computation time. It was therefore possible to perform many fits with different parameters, corrections, and portions of the spectrum.

Before considering the main results we consider the effect of the extinction correction on the fitted spectra, and in particular its effect on the Debye–Waller factor (assuming no anharmonicity term). We show in Table 3 the results of nine-parameter fits with (*a*) no correction, (*b*) with a self-shielding correction applied with the calculated cross section and (*c*) with the extinction parameter X_{11} fixed at the best value deduced from the low-order peaks; (*d*) is a ten-parameter fit where the

Table 2. *Peak intensities by direct summation*

Order	$\sin\theta/\lambda$ (Å^{-1})	λ (Å)	Area (barn sterad^{-1} μs)	$\sigma \exp(-2W)/4\pi$ (barn sterad^{-1}) No correction	Self-shielding correction	Extinction parameter
111	0·245	3·94	301 (23)	0·135 (0·015)	0·373 (0·041)	—
200	0·283	3·41	209 (12)	0·222 (0·014)	0·388 (0·022)	0·740 (0·046)
220	0·400	2·42	203 (8)	0·432 (0·020)	0·645 (0·028)	0·643 (0·029)
311	0·469	2·06	245 (4)	0·495 (0·010)	0·811 (0·014)	0·740 (0·014)
222	0·490	1·97	70·9 (4)	0·510 (0·028)	0·595 (0·033)	0·561 (0·034)
400	0·566	1·71	24·9 (3)	0·593 (0·048)	0·639 (0·052)	0·615 (0·056)
331	0·616	1·57	91·3 (2·2)	0·549 (0·014)	0·691 (0·016)	0·608 (0·016)
420	0·632	1·53	79·6 (2·2)	0·532 (0·015)	0·658 (0·018)	0·583 (0·018)
422	0·693	1·39	56·0 (1·7)	0·538 (0·015)	0·634 (0·020)	0·570 (0·022)
333, 511	0·735	1·31	56·7 (0·7)	0·517 (0·007)	0·619 (0·007)	0·656 (0·007)
440	0·800	1·21	14·2 (0·9)	0·486 (0·031)	0·512 (0·032)	0·493 (0·032)

extinction parameter is allowed to vary in the least-squares fit. In each case fits were performed on two spectra; spectrum *A* from 2·1 Å to 0·5 Å which corresponds to both parts of Fig. 9 and spectrum *B* from 1·3 Å to 0·5 Å which corresponds to the upper half only of this figure. It is seen that in the case of the full spectrum *A*, the two fits with the fixed self-shielding and extinction corrections give similar values of the harmonic coefficient of 0·36 and 0·34 Å^2 respectively. However these values are much larger than the 0·24 Å^2 given by the fit without any correction or the 0·30 Å^2 given by the fitted extinction parameter $X_{11}=1{\cdot}2$ – just over half the value giving good agreement with the low-order peaks. In the case of the lower wavelength spectrum *B* the correction has much less importance and all the coefficients are within 0·1 Å^2 or so. We conclude that for spectra measured above 1·3 Å the self-shielding correction is likely to be essential. However the parametrized extinction correction fitted from the low orders gives equally good fits. We test both approaches by using the parametric extinction correction in the fits with no anharmonic term in Table 4, and using the more objective calculated self-shielding correction in Table 5 where we consider the effects of including an anharmonic term.

In Table 4 we consider several nine-parameter fits, including the harmonic coefficient *B*, but excluding any anharmonic term, to various parts of the time-of-flight spectrum. As before, spectra *A* and *B* correspond to the full spectrum of Fig. 9 and the upper half respectively. Spectrum *C* corresponds roughly with the right-hand half of the upper half of the figure, and spectrum *D* with the right-hand quarter of the upper half of the figure. Spectrum *E* corresponds to the lower half of the figure. In all cases the extinction correction fixed from the low-order intensities is included.

If the background parameters are considered first, it is seen that the flat contribution to the background

Table 3. *Tests of the extinction correction*

	Parameter	(*a*) No correction	(*b*) Self-shielding correction	(*c*) Fixed extinction correction	(*d*) Fitted extinction correction
Spectrum *A* (2·1 to 0·5 Å)	B (Å^2)	0·2469	0·3578 (0·0002)	0·3439 (0·0004)	0·3050 (0·0007)
(0·46 to 2·09 Å^{-1})	χ^2	0·186	0·161	0·168	0·141
Spectrum *B* (1·3 to 0·5 Å)	B (Å^2)	0·3207 (0·0004)	0·3232 (0·00015)	0·3341 (0·0005)	
(0·75 to 2·09 Å^{-1})	χ^2	0·178		0·183	

Table 4. *Profile-analysis fits without anharmonicity*

Spectrum	*A*	*B*	*C*	*D*	*E*
sin θ/λ range: lower (Å^{-1})	0·46	0·75	1·11	1·36	0·46
upper (Å^{-1})	2·09	2·09	2·09	2·09	0·75
Wavelength range: upper (Å)	2·109	1·284	0·873	0·711	2·109
lower (Å)	0·463	0·463	0·463	0·463	1·284
Number of channels:	949	474	237	143	475
Background parameters:					
$X_1\simeq(d\sigma/d\Omega)_{inc}$ (barn sterad^{-1})	0·705 (0·002)	0·709 (0·003)	0·852 (0·002)	0·809 (0·002)	0·701 (0·003)
$X_2\simeq(d\sigma/d\Omega)_{coh}$ (barn sterad^{-1})	2·98 (0·002)	3·23 (0·03)	5·22 (0·02)	6·49 (0·02)	3·27 (0·02)
$X_3\simeq B_{Ni}$ (Å^2)	0·1821 (0·0007)	0·1541 (0·0007)	0·043 (0·002)	0·039 (0·003)	0·158 (0·003)
Lineshape parameters:					
X_4 Assymetry $\sigma_{t>}/\sigma_{t<}$	1·626 (0·007)	1·57 (0·01)	1·389 (0·001)	1·1427 (0·0002)	1·57 (0·01)
X_5 Width (FWHH) μs (Å)$^{-1}$	13·20 (0·05)	13·64 (0·05)	14·43 (0·07)	14·89 (0·02)	13·62 (0·08)
Position parameters:					
X_6 Lattice parameter Å	3·52313 (0·00009)	3·5262 (0·0002)	3·5225 (0·0002)	3·5250 (0·0005)	3·51844 (0·00001)
X_7 Time delay (μs)	5·32 (0·02)	6·30 (0·02)	5·65 (0·02)	6·38 (0·02)	3·18 (0·02)
Intensity parameters:					
$X_8\simeq(d\sigma/d\Omega)_{coh}$ (barn sterad^{-1})	0·795 (0·001)	0·804 (0·002)	0·745 (0·002)	1·14 (0·01)	0·866 (0·001)
$X_9=B_{Ni}$ (Å^2)	0·344 (0·001)	0·334 (0·001)	0·2960 (0·0007)	0·381 (0·002)	0·506 (0·002)
Fit quality χ^2	0·168	0·183	0·179	0·187	0·092

at 0·7 barn sterad^{-1} is nearly twice the accepted value of the incoherent cross section for nickel of 0·366 barn sterad^{-1}. This fact is not understood by us, since the coherent-scattering spectrum agrees within 20% with that predicted from the coherent cross section, suggesting that our absolute intensity calibration using vanadium is not seriously in error. Also the general time independence of the incoherent background suggests that the background subtraction has been reasonably precise. We suspect that the most probable explanation lies in imperfect alignment of the cadmium shield over the resin-glued sample holder.

The increase in the apparent background at short wavelengths is well fitted by our inelastic contribution discussed in *The profile-analysis procedure* § (1). The derived coherent cross section $X_2 \simeq 3$ barn sterad^{-1} for fit A is of the same order of magnitude as the accepted value of 1·07 barn sterad^{-1}, while the apparent harmonic coefficient of 0·18 Å^2 is also of the right order, especially as the value should be compared with that measured at high sin θ/λ. The more limited fits, B, C and D, give less useful information from the background fits since the parameters become highly correlated over a limited sin θ/λ range. As a method for measuring the Debye–Waller factor, the increase in background from inelasticity certainly gives a quick method valid over the limited sin θ/λ range, but depends too much on the assumed incoherent approximation to be reliable for accurate work.

The line-shape asymmetry parameter X_4 has values between 1·6 and 1·4 and clearly decreases with increasing sin θ/λ. It would perhaps be worth while introduc-

Table 5. *Profile-analysis fits including the anharmonic term*

Spectrum	A: (2·109 to 0·463 Å) (0·46 to 2·09 Å^{-1})			B: (1·284 to 0·463 Å) (0·75 to 2·09 Å^{-1})		
$X_8=(d\sigma/d\Omega)_{coh}$ (barn sterad^{-1})	0·7954 (0·0005)	0·8083 (0·0010)	0·8354 (0·0005)	0·8042 (0·0007)	0·8064 (0·0009)	0·8897 (0·0012)
$X_9=B_{Ni}$ (Å^2)	0·3439 (0·0004)	0·3696 (0·0006)	(0·42)	(0·334) (0·0005)	0·331* (0·001)	(0·42)
$X_{10}=C_{Ni}$ (Å^4)	(0)	−0·0123 (0·0006)	−0·04030 (0·00001)	(0)	0·00309* (0·00002)	−0·0297 0·0001
Fit quality χ^2	0·168	0·156	0·167	0·183	0·181	0·187

* A value B of 0·33 Å^2 around sin $\theta/\lambda=1{\cdot}5$ Å^{-1} with a B of 0·37 at small sin θ/λ is equivalent to $C \simeq -0{\cdot}007$ Å^4.

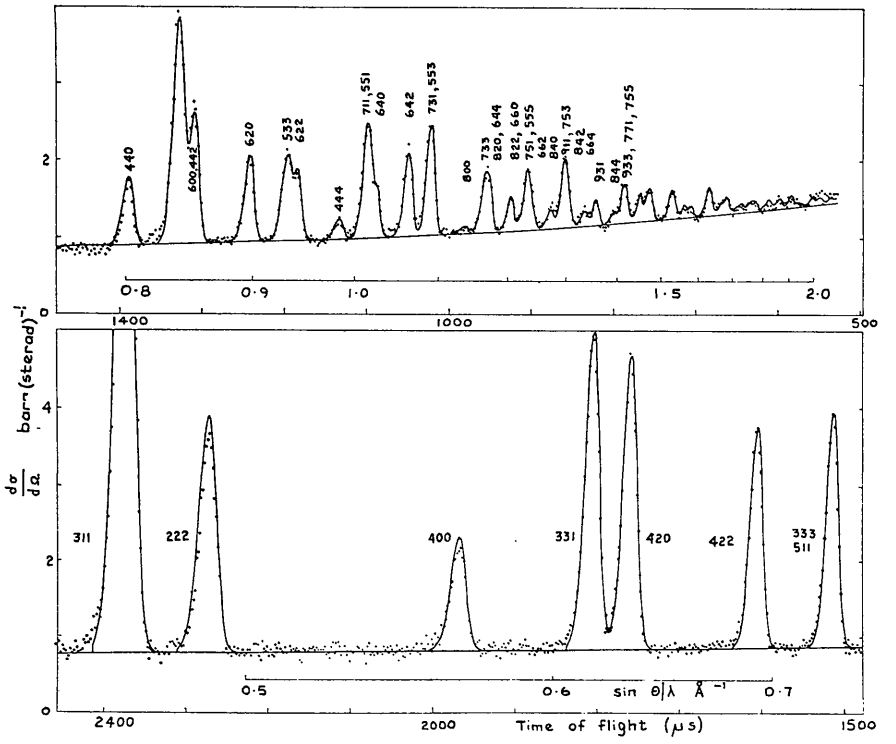

Fig. 9. A profile-analysis refinement of nickel powder data. The solid curve has a harmonic coefficient $B=0{\cdot}37$ Å^2 with an anharmonic term $C=-0{\cdot}012$ Å . It contains an extinction parameter derived from the lowest-order peaks.

ing a further parameter to describe this decrease. The line width is shown to be rather accurately proportional to wavelength, the width parameter X_5 varying only between 13·2 to 14·4 μs Å^{-1}. This confirms the analysis of *The profile-analysis procedure* § (2). The constant is of course less than the intrinsic thermalization width of 7 μs Å^{-1} because of the angular and distance broadening contributions.

The lattice parameter X_6 is seen to be extremely well determined by the powder-profile method. The fit *A* gave a value 3·52313 ± 0·00004 Å within 2×10^{-4} of the accepted value for this sample of 3·5237 Å. Relative values of lattice parameters may be made extremely accurately since they would depend only on the total flight path which can be very precisely measured and the time-of-flight zero which may be deduced within a microsecond or so from the form of the spectrum itself. An absolute determination of a lattice parameter would require a careful analysis of the delays in the neutron pulse caused by the thermalization process. For example the origin of the 6 μs wavelength-independent delay given by parameter X_7 is not clear to us. Another difficulty is given by the intensity of the coherent spectrum which is around 20% lower than given from the accepted coherent cross section of 1·066 barn sterad^{-1}.

The harmonic coefficients given by our pulsed powder measurements are lower than the recent fixed-wavelength measurements of 0·426 ± 0·009 Å^2 from neutron measurements of Cooper & Taylor (1969) or of 0·37 ± 0·02 Å^2 from X-ray measurements of Inkinen & Suortti (1964). We also see that the coefficient decreases from 0·34 Å^2 in fit *A* to 0·30 in fit *C* as the range of the fit is confined to higher values of sin θ/λ. This effect naturally suggests the inclusion of the anharmonicity term which reduces the effective harmonic coefficient as sin θ/λ is increased. Such a term will be considered in the next section.

Lastly we note the low statistical errors given by the profile analysis fits even those from the relatively short spectra of *B* or *C*. It has been noted from fixed-wavelength neutron profile studies that it is the high sin θ/λ region of highly overlapping peaks which leads to precise determinations of structural parameters (Hewat, 1973). This is certainly confirmed in our example by the high precision of the parameters deduced from spectrum *C*. The fit quality is shown by the solid line in Fig. 10, which is a fit to spectrum *A* having *B* = 0·34 Å^2. The dashed line shows the sensitivity of the high sin θ/λ region of the spectrum to the value of the Debye–Waller factor. If the value of *B* is increased say to 0·42 Å^2, and the intensity of the 422 peak at 0·7 Å^{-1} is adjusted to remain unchanged, then the intensities around 1·5 Å^{-1} are reduced by 30%, and are very easily observed.

The effect of anharmonicity

The conventional harmonic coefficient *B* represents physically the spatial dependence of the atoms arising from their thermal vibrations in a harmonic potential. In practice this potential will contain an anharmonic term γ related to the fourth power of the atomic displacements *u*,

$$V = V_0 + \tfrac{1}{2}\alpha u^2 + \gamma u^4. \qquad (42)$$

There may also be other anisotropic terms showing the shape of the potential, but these are of high order and so small in face-centred cubic structures where the environment on any atom is rather symmetrical. Strictly the solution of the effective Debye–Waller factor for this potential is a complex problem since the

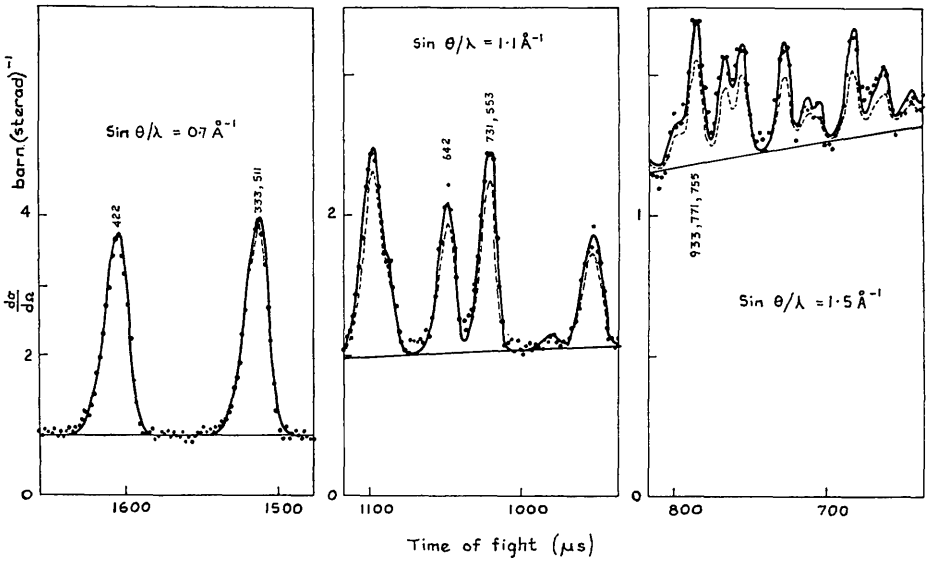

Fig. 10. Examples of the profile analysis refinement with *B* = 0·34 Å^2 (full line) and *B* = 0·42 Å^2 (dashed line).

detailed phonon eigenvectors must be known. However Willis (1969) has shown that within the approximation that the lattice is composed of uncoupled anharmonic oscillators, the effective Debye–Waller parameter is

$$2W=Q^2\frac{kT}{\alpha_0}+Q^4(kT)^3\frac{2\gamma}{\alpha^4}. \quad (43)$$

Writing this in the form

$$2W=2B\left(\frac{\sin\theta}{\lambda}\right)^2+2C\left(\frac{\sin\theta}{\lambda}\right)^4, \quad (44)$$

we have the relations,

$$B=\tfrac{1}{2}(4\pi)^2.\frac{kT}{\alpha} \text{ and } C=\tfrac{1}{2}(4\pi)^4(kT)^3\frac{2\gamma}{\alpha^4}. \quad (45)$$

Since γ is likely to be negative, the additional term is also negative and tends to reduce the effective term B. This is exactly in accord with the fits presented in the previous section where the fitted value of B decreased as the sin θ/λ range covered by the fit was increased.

We show in Table 5 results from ten-parameter fits including the anharmonic term as an adjustable parameter X_{10}. Fits were made to spectrum A covering all of Fig. 9 and to spectrum B covering only the upper half of the figure. In all cases the self-shielding correction was applied with the calculated cross section. It is seen that inclusion of the anharmonic parameter results in a considerable improvement in the quality of fit χ^2. Both A and B spectra suggest an anharmonic term of order $C=0{\cdot}007$ Å^4 and also increase the harmonic term B to 0·37 Å^2 in excellent agreement with the X-ray result $B=0{\cdot}37\pm0{\cdot}02$ Å^2 of Inkinen & Suortti (1964) and the theoretical value $B=0{\cdot}38$ Å^2 from Barron & Smith (1966). Constraining B to this theoretical value gives only a slight increase in the anharmonic term. Constraining B to the neutron measurement $B=$ 0·42 Å^2 gives a substantially increased anharmonic coefficient. The full line in Fig. 9 shows a fit to spectrum A with the values $B=0{\cdot}37$ Å^2 and $C=-0{\cdot}012$ Å^4 obtained by applying the ten-parameter fit with the fixed extinction correction.

We conclude best values for the harmonic and anharmonic coefficients:

$$B=0{\cdot}37\pm0{\cdot}1 \text{ Å}^2$$
$$C=-0{\cdot}010\pm0{\cdot}005 \text{ Å}^4. \quad (46)$$

Using equations (45) we may deduce from their values the parameters of the potential α and γ of

$$\alpha=8{\cdot}8\pm0{\cdot}2\times10^{-12} \text{ erg Å}^2$$
$$\gamma=-44\pm20\times10^{-12} \text{ erg Å}^4. \quad (47)$$

This second-order term has the right sign and magnitude, but is clearly only rather inaccurately determined from our results unless a value is assumed for the second-order term B in the Debye–Waller factor. Measurements as a function of temperature are planned to obtain greater accuracy in these higher-order terms.

Conclusions

It has been shown that pulsed neutron powder diffraction using an electron LINAC source and back-scattering geometry, enable useful powder profiles to be obtained at scattering vectors up to 24 Å^{-1} (sin $\theta/\lambda=$ 2 Å^{-1}). The relatively short pulses and high intensity obtained at short wavelengths from LINAC sources enable both signal and percentage resolution to be maintained at the highest scattering vectors. A pattern from nickel powder was refined using profile-analysis techniques. The best fits were obtained with a Debye–Waller factor including a term to fourth order in sin θ/λ expected from anharmonic theory. The associated conventional second-order term had the value $B=0{\cdot}37$ Å^2 in good agreement with X-ray and theoretical values.

References

Barron, H. W. T. & Smith, T. (1966). *J. Phys. Chem. Solids*, **27**, 1951–1952.

Becker, P. J. & Coppens, P. (1974). *Acta Cryst.* A**30**, 129–153.

Brugger, R. M., Bennion, R. B. & Worlton, T. G. (1967). *Phys. Lett.* **24A**, 714.

Buras, B. (1963). *Nukleonika*, **8**, 259–260.

Buras, B. & Holas, A. (1966). Report INR 745/II/P5. Institute of Nuclear Research, Warsaw.

Buras, B., Leciejewicz, J., Nite, W., Sosnowska, I., Sosnowski, J. & Shapiro, F. (1964). *Nukleonika*, **9**, 523–535.

Chipman, D. R. & Paskin, A. (1959). *J. Appl. Phys.* **30**, 1992–2001.

Clarke, J. H. (1975). Report AERE – R2182.

Cooper, M. J. & Taylor, R. I. (1969). *Acta Cryst.* A**25**, 714–715.

Day, D. H. & Sinclair, R. N. (1969). *Nucl. Instrum. Meth.* **72**, 237–253.

Egelstaff, P. A. (1961). *Proc. Symp. Neutron time-of-flight methods EANDC Saclay*, pp. 69–74.

Egelstaff, P. A. &Squires, G. L. (1954). *Third Congress of the International Union of Crystallography*, Paris. *Résumé des Communications*, p. 60; *Acta Cryst.* **7**, 673.

Fluharty, R. G., Simpson, F. B., Russell, G. J. & Menzel, J. H. (1969). *Nucl. Sci. Eng.* **35**, 45–69.

Graham, K. F. & Carpenter, J. M. (1970). *Nucl. Instrum. Meth.* **85**, 163–171.

Hewat, A. W. (1973). *J. Phys. C: Solid State Phys.* **6**, 2559–2572.

Inkinen, O. & Suortti, P. (1964). *Ann. Acad. Sci. Fenn.* **AVI**, 147.

Kimura, M., Sugawara, M., Oyamada, M., Yamada, Y., Tomiyoshi, S., Suzuki, T., Watanabe, N. & Takeda, S. (1969). *Nucl. Instrum. Meth.* **71**, 102–110.

Lebech, B. & Mikke, K. (1972). *J. Phys. Chem. Solids*, **33**, 1651–1663.

Lowde, R. D. (1956). *Acta Cryst.* **9**, 151–155.

Marshall, W. & Lovesey, S. (1971). *Theory of Thermal Neutron Scattering*. Oxford Univ. Press.

Maier-Leibnitz, H. & Springer, T. (1966). *Ann. Rev. Nucl. Sci.* **16**, 207–262.

MOORE, M. J., KASPER, J. S. & MENZEL, J. M. (1968). *Nature, Lond.* **219**, 848–849.
PAALMAN, H. H. & PINGS, C. J. (1962). *J. Appl. Phys.* **33** 2635–2639.
POWELL, M. J. D. (1965). *Comput. J.* **7**, 303–307.
REICHELT, J. M. A. & RODGERS, A. L. (1966). *Nucl. Instrum. Meth.* **45**, 245–249.
RIETVELD, H. M. (1969). *J. Appl. Cryst.* **2**, 65–71.
SCHWARTZ, L. H. (1966). *Nucl. Instrum. Meth.* **42**, 81–86.
SINCLAIR, R. N., JOHNSON, D. A. G., DORE, J. C., CLARKE, J. H. & WRIGHT, A. C. (1974). *Nucl. Instrum. Meth.* **117**, 445–454.
STEICHELE, E. & ARNOLD, P. (1973). *Phys. Lett.* **44A**, 165–166.
WILLIS, B. T. M. (1969). *Acta Cryst.* A**25**, 277–300.
ZACHARIASEN, W. H. (1967). *Acta Cryst.* **23**, 558–564.

Acta Cryst. (1976). A**32**, 409

Application of Theoretical Intensity Distribution Curves to the Analysis of Disordered ZnS–CdS and ZnS–ZnSe Crystals*

BY B. PAŁOSZ AND J. PRZEDMOJSKI

Warsaw Technical University, Institute of Physics, Koszykowa 75, 00-662 *Warszawa, Poland*

(*Received* 22 *January* 1975; *accepted* 11 *September* 1975)

The possibility is discussed of applying the theoretical intensity distribution formulae to the structural analysis of solid solution crystals of ZnS–CdS and ZnS–ZnSe with stacking faults. It is pointed out that the irregular shape of the photometric curves, the appearance of intensity maxima connected with areas of disordered type structure, and splitting of the diffuse reflexions, renders impossible the application of theoretical intensity formulae. Theoretical intensity curves, obtained for the model of a structure with stacking faults, are proposed for structural analysis.

Introduction

The ZnS crystals can be divided into two structural groups: polytypes, and structures with stacking faults. The structural analysis of polytypes consists of establishing the layer sequence periodicity in the unit cell thus determining completely the structure. The analysis of structures with stacking faults is much more complicated and calls for the introduction of parameters describing the degree of disorder in the arrangement of layers. The analysis of such structures can be of an approximate nature only, since it describes an infinite, statistically repeatable, sequence of layers forming the crystal. Polytypes usually occur in small areas of larger crystals or in the form of single crystals of macroscopic size (Brafman & Steinberger, 1966; Brafman, Alexander & Steinberger, 1967; Mardix, Kalman & Steinberger, 1968; Alexander, Kalman, Mardix & Steinberger, 1970; Rai, 1971*a*, 1972). Polytypes are usually accompanied by areas with stacking faults (Singer, 1963*a*; Rai & Krishna, 1968). In the investigated ZnS–CdS and ZnS–ZnSe crystals, areas of about 5 mm^2 showing similar stacking faults were found.

Polytype formation mechanisms suggested in the literature (Daniels, 1966; Mardix *et al.*, 1968; Alexander *et al.*, 1970; Rai, 1971*a*, *b*) are based on the analysis of known pure polytypes. Structures with stacking faults may be considered as probable transition stages between pure polytype structures; hence the analysis of these structures may serve to explain the polytype growth mechanism.

Experimental results

Crystals of ZnS–CdS and ZnS–ZnSe solid solutions were investigated by the oscillating-crystal method in a range of 15° around the *c* axis with Cu $K\alpha$ radiation. The selected samples consisted of needles cut parallel to the *c* axis, measuring 2–4 mm in length and about 0·5 mm in diameter. The X-ray beam was of 0·5 mm diameter. On the *c* axis oscillation photograph a 10.*L* row of spots was obtained and subsequently in the intensity–*L*/*m* coordinate system the photometric curve was plotted, where *m* denotes the number of layers in the unit cell; *e.g.* the reflexion 10.1 for the structure 3*C* remains in the position $\frac{1}{3}=0{\cdot}333$, the reflexion 10.1 of the structure 15*H* in position $\frac{1}{15}=0{\cdot}0667$ *etc.* On the photometric curves broadened maxima were found in positions corresponding with 10.*L* reflexions of the 2*H*, 3*C*, 4*H*, 6*H* and 10*H* structures indicating that the latter polytype structural fragments appear in the crystal. The background observed on the photometric curves originates from disordered structure fragments. The analysis of the photometric curves of 10.*L* rows of spots of X-ray pattern for crystals oscillating around the *c* axis showed the occurrence of the following structures: 2*H*+disorder (Fig. 1), 3*C*+disorder (Fig. 2), 4*H*+disorder (Fig. 3), 6*H*+disorder (Fig. 4), 10*H*+disorder, 2*H*+4*H*+

* This work was sponsored by the Institute of Physics of the Polish Academy of Science.